

# Bluff-Body Flow Control via Two Types of Dielectric Barrier Discharge Plasma Actuation

Alexey V. Kozlov\* and Flint O. Thomas†  
University of Notre Dame, Notre Dame, Indiana 46556

DOI: 10.2514/1.J050793

In this experimental study, dielectric barrier discharge plasma actuators are used to control vortex shedding from circular cylinder models in uniform crossflow at a Reynolds number of  $Re_D = 85,000$ . Circular cylinders in crossflow are chosen for study, since they represent a generic flow geometry that is similar in all essential aspects to a landing gear oleo or strut. The focus of the flow control is the elimination/minimization of the unsteady flow separation from the models and the associated large-scale wake vorticity. Two actuation strategies are used: spanwise- and streamwise-oriented plasma actuators. Global flow visualization, near-field microphone measurements, and detailed study of the near wake using laser Doppler velocimetry are presented in the paper. Both spanwise and streamwise actuators are shown to significantly suppress Kármán shedding and provide near-field unsteady pressure fluctuation reductions of 11.2 and 14.2 dB, respectively, within the frequency band associated with shedding.

## Nomenclature

$D$	= cylinder diameter
$d$	= cylinder wall thickness
$f_s$	= vortex shedding frequency
$\ell_s$	= spatial extent of separated flow
$Re_D$	= Reynolds number based on cylinder diameter
$St_D$	= Strouhal number based on cylinder diameter
$U$	= streamwise mean velocity component
$U_\infty$	= freestream velocity
$u$	= streamwise fluctuating velocity component
$V$	= cross-stream mean velocity component
$v$	= cross-stream fluctuating velocity component
$x$	= streamwise spatial coordinate, measured from the cylinder axis
$y$	= cross-stream spatial coordinate, measured from the cylinder axis
$z$	= spanwise electrode spacing

## I. Introduction

AIRCRAFT noise will remain a constraint on the growth of the commercial air transportation system unless new technologies can be developed to reduce community noise impact. With the use of quieter high-bypass-ratio engines, airframe noise now represents a primary noise source for large- and medium-size civil transport aircraft on landing approach. Through a combination of both aircraft flyover tests and wind-tunnel experiments, the deployed landing gears have been identified as one primary source of airframe noise [1–4]. As a result, there has been considerable effort to model and control landing gear noise [5–10]. The inherent bluff-body characteristics of landing gears give rise to large-scale unsteady flow separation that results in noise production through unsteady wake flow and large-scale vortex instability and deformation [11]. Of key importance is the unsteady wake interaction with downstream gear

components and other undercarriage elements. For this reason, the tandem cylinder in crossflow represents a canonical flowfield geometry that is relevant to the landing gear noise-generation process and has been the focus of several recent studies [12–16]. It is clear that any bluff-body flow control strategy, either active or passive, that eliminates or minimizes flow separation and the associated unsteady multiple wake interactions with downstream airframe components can have a significant effect on airframe noise.

Because of numerous technological applications, bluff-body flow control by both active and passive means has been an active research area as reviewed by Choi et al. [17]. Much of this work has involved the circular cylinder in uniform crossflow and has been focused on drag reduction. Passive methods include use of distributed roughness, helical wires, and various types of splitter plates. The use of a secondary flow control cylinder positioned in close proximity to the primary cylinder can serve to minimize the global instability that gives rise to vortex shedding. Active methods of flow control include rotary, transverse, or longitudinal oscillation of the cylinder itself as well as both steady and time-dependent surface blowing/suction. The use of synthetic jets at high forcing frequency was found to produce drag reduction for a cylinder in crossflow [18].

In this paper, the results of cylinder flow control experiments using two types of surface-mounted dielectric barrier discharge (DBD) plasma actuators are presented. The work is motivated by the desire to eliminate or minimize unsteady vortex shedding for later application to tandem-cylinder active flow control. Numerous studies as reviewed in [19,20] have demonstrated DBD plasma actuators are ideally suited to separation control for a wide variety of practical aerodynamic applications. Advantages of the DBD plasma actuator for aerodynamic control include sufficient actuator authority even at high Reynolds numbers [21], excellent dynamic response, low required energy input, robust with no moving parts, inexpensive, capable of both steady and unsteady actuation with a wide range of unsteady actuation strategies implemented in software, and perhaps most importantly, can be relatively easily retrofitted to the current generation of commercial transport aircraft. In contrast, suction or blowing requires the incorporation of a complex air bleed ducting systems making a retrofit impractical.

In Thomas et al. [22] four surface-mounted DBD plasma actuators were used to control vortex shedding from a circular cylinder model in uniform crossflow. The cylinder in crossflow was viewed as a generically relevant flow geometry that is similar in all essential aspects to a landing gear oleo or strut. The study used both quasi-steady and unsteady (pulsed) plasma actuation to eliminate vortex shedding from the cylinder at approximately  $Re_D = 30,000$ . As a consequence, near-field pressure fluctuations associated with shedding were significantly reduced. Large-eddy simulation of the

Presented at the 15th AIAA/CEAS Aeroacoustics Conference, Miami, FL, 11–13 May 2009; received 24 July 2010; revision received 28 January 2011; accepted for publication 19 March 2011. Copyright © 2011 by the American Institute of Aeronautics and Astronautics, Inc. All rights reserved. Copies of this paper may be made for personal or internal use, on condition that the copier pay the \$10.00 per-copy fee to the Copyright Clearance Center, Inc., 222 Rosewood Drive, Danvers, MA 01923; include the code 0001-1452/11 and \$10.00 in correspondence with the CCC.

\*Postdoctoral Research Associate, Institute for Flow Physics and Control, Department of Aerospace and Mechanical Engineering.

†Professor, Institute for Flow Physics and Control, Department of Aerospace and Mechanical Engineering. Associate Fellow AIAA.

same plasma flow control experiment reported in [22] was performed by Kim and Wang [23]. In their paper, the influence of the plasma actuation was modeled as a body force in the governing equations. Good agreement between the simulations and experiment were reported for both quasi-steady and pulsed plasma actuation cases. This study showed that large-scale vortex shedding is virtually eliminated by both steady and unsteady actuation, and that the mean drag as well as drag and lift fluctuations are also significantly reduced. The frequency of unsteady plasma actuation was found to have a large effect on the control performance with the Strouhal number range  $1 < St_D < 1.5$  yielding optimum results. In recent work reported by Huang and Li [24], plasma actuation has also been explored in order to reduce broadband noise from a cylinder wake interaction with a downstream torque link.

This paper extends the cylinder flow control work reported in [22] by using new DBD plasma actuator designs of higher authority developed in the course of the optimization study reported in [21]. This allows plasma flow control at significantly higher  $Re_D$ . In addition, two different types of plasma actuator configurations are investigated and their flow control performance contrasted. In the first, actuators with electrodes oriented in the spanwise direction are employed. These surface-mounted DBD plasma actuators are similar to those used in [22] but due to the improvement in actuator design, a larger plasma-forming region is formed and, consequently, only two (instead of four) are used at higher  $Re_D$ . In the second approach, 15 surface-mounted actuators with electrodes oriented in the streamwise direction are used. It will be shown that these are employed in order to form plasma-induced streamwise vortices and this arrangement will be called a plasma streamwise vortex generator (PSVG). These will be shown to introduce streamwise vorticity into the nascent cylinder wake, which has the effect of promoting rapid wake mixing. The use of DBD plasma-induced streamwise vorticity for aeroacoustic control of a low-speed cavity resonance is reported in [25].

In both actuator arrangements used in this study the goal is the minimization of unsteady large-scale vortex shedding and the associated near-field pressure fluctuations. To document this, microphone measurements obtained in a large open-jet anechoic wind-tunnel facility are also presented. The bluff-body wake control achieved in these experiments will set the stage for implementation of DBD plasma actuators in both a tandem-cylinder configuration and a realistic landing gear geometry. Before describing the flow control experiments a brief review of the DBD plasma actuator is provided.

## II. Dielectric Barrier Discharge Plasma Actuators

A dielectric barrier discharge forms the basis for the plasma actuators used in this investigation [26]. This plasma actuator can sustain a large volume discharge at atmospheric pressure *without arcing*, since it is inherently self-limiting. The basic characteristics of DBD plasma actuators are described in Enloe et al. [27,28]. For a review of flow control applications of DBD plasma actuators the reader is referred to Corke et al. [19] and Moreau [20].

As shown in Fig. 1, a plasma actuator is a relatively simple device consisting of two electrodes that are separated by a dielectric barrier material. The two electrodes are usually given a slight overlap. When a sufficiently high ac input voltage is supplied to the electrodes the dielectric barrier discharge ignites. The physical structure of DBD is

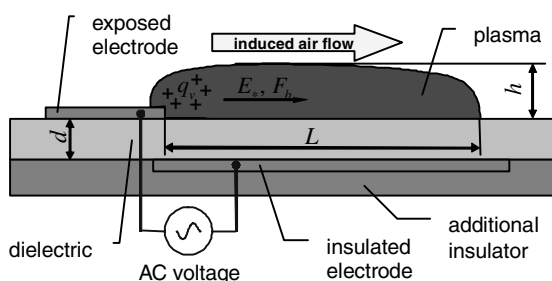


Fig. 1 Schematic of the DBD plasma actuator.

described in Gibalov and Pietsch [29]. The mechanism of charge multiplication and air ionization is similar to the corona discharge process described in Raizer [30]. Ionization generally starts at the edge of the electrode that is exposed to the air where the intensity of the electric field has its largest value. When the magnitude of this electric field is high enough, electron avalanches followed by streamer formation are produced. Streamers are thin, highly ionized channels between the electrodes with a lifetime of the order of 10 ns. They begin at the exposed electrode edge and terminate at the dielectric surface. Because of their relatively high conductivity, the streamers efficiently transfer electric charge from the exposed electrode to the plasma volume near the dielectric surface. Since this volume charge has the same sign as the charge of the exposed electrode, the electrostatic force repels it from the exposed electrode and it is attracted to the dielectric surface above the covered electrode. This buildup of surface charge on the dielectric surface opposes the applied voltage and gives the plasma discharge its self-limiting character. That is, the plasma is extinguished unless the magnitude of the applied voltage continuously increases. The charge transfer process repeats in the opposite direction during the second half of the ac cycle (i.e., from dielectric surface back to the exposed electrode).

As a result of ion collisions with neutrals, the formation of the plasma gives rise to an effective body force on the ambient air. It is the resulting coupling of directed momentum to the surrounding air that forms the basis for flow control strategies. Although the direction of charge transfer varies during the two halves of the ac cycle, the body force always has the same direction. Of importance is the fact that the body force and induced velocity can be tailored through the design of the electrode arrangement, which controls the spatial electric field. Thomas et al. [21] report a plasma actuator parametric optimization study that demonstrates the achievement of body forces an order of magnitude greater than those attained in previous plasma flow control studies that typically used thin Kapton film as the dielectric barrier. Schatzman and Thomas [31] recently demonstrated the effectiveness of PSVG for turbulent boundary-layer separation control. This suggests the possibility of using PSVG for cylinder flow control, which is one focus of this paper.

## III. Cylinder Models and Experimental Facilities

The flow control experiments were performed in one of the low-turbulence, subsonic, in-draft wind tunnels located at the Hessert Laboratory for Aerospace Research at the University of Notre Dame. The wind tunnel has an inlet contraction ratio of 20:1. A series of 12 turbulence-management screens at the front of the inlet give rise to tunnel freestream turbulence levels of less than 0.1% (0.06% for frequencies above 10 Hz). Experiments are performed in a test section of 0.610 m square cross section and 1.82 m in length. One sidewall and ceiling has optical access for nonintrusive laser flowfield diagnostics (laser Doppler anemometry) and flow visualization.

Flow visualization images are obtained using a Photron FASTCAM SA1.1 high-speed digital camera. Continuous olive oil fog streaklines consisting of nominally 1- $\mu\text{m}$ -diam droplets are introduced upstream of the wind-tunnel inlet contraction. The fog streaklines are contained in the spanwise center plane of the wind-tunnel test section where they are illuminated by a 542 nm, 2 W solid-state laser (Excel quantum laser with MPC6000 power supply). The olive oil fog droplets are generated by a Dantec particle seeder.

Nonintrusive near-wake velocity measurements were conducted using a Dantec Dynamics laser Doppler anemometry (LDA) system with Fiber Flow optical system, BSA-F60 Flow Processor, BSA Flow Software version 4.40.02, and Spectra-Physics Stabilite 2017 argon-ion laser. The fiber optic LDA system is operated in 180° backscatter mode. The LDA optical configuration produced a probe volume of dimension 0.2 mm in both the streamwise and cross-stream directions. This defines the effective spatial resolution for the LDA measurements. To position the fiber optic head, a three-component stepper motor traverse system with Aerotech Unidex11 motion controller is used. The same 1- $\mu\text{m}$ -diam olive oil droplets

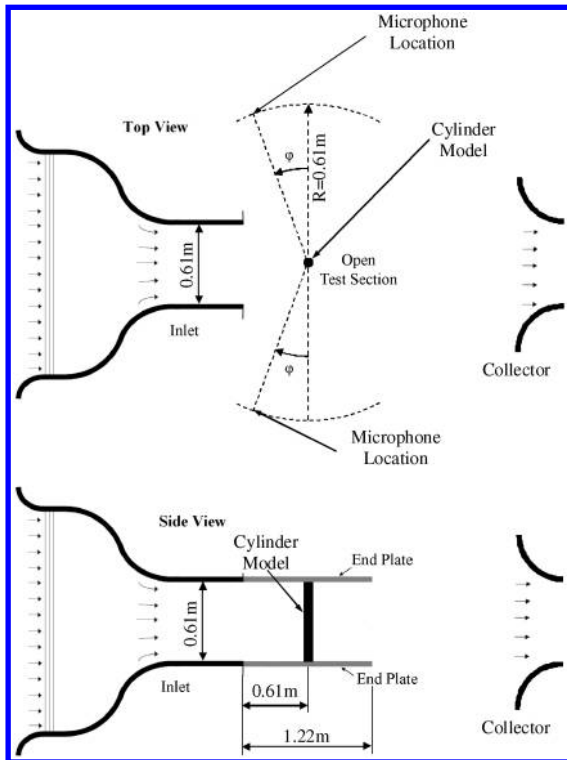


Fig. 2 Schematic of the experimental arrangement in the anechoic wind tunnel.

used for flow visualization were used as LDA seed particles. The LDA mean velocity measurements have a  $\pm 3.3\%$  relative uncertainty at 95% confidence. Turbulence intensity measurements have a relative uncertainty of  $\pm 3.4\%$ .

Complementary acoustic measurements were conducted in a separate anechoic in-draft wind-tunnel facility also located in the Hessert Laboratory at the University of Notre Dame. The open-jet wind-tunnel facility is contained within an anechoic chamber that is 7.9 m long, 6.1 m wide and 2.44 m in height. The room treatment is rated to absorb 99% of incident sound waves above 100 Hz, giving rise to an anechoic free-field environment for higher frequencies. A schematic of the experimental arrangement is shown in Fig. 2. The wind tunnel draws in ambient laboratory air through an inlet with multiple turbulence-management screens and a contraction ratio of 8:1. The exit of the contraction is 0.61 m by 0.61 m in cross section, and defines the beginning of the open-jet test section. The cylinder model is mounted vertically in the test section 0.61 m downstream from the contraction exit. The flow in the test section is constrained from the upper and lower sides by a pair of plywood endplates. Two free shear layers are formed by the flow exiting the inlet on the sides of the test section not constrained by the endplates. This creates a two dimensional open-jet test section, which allows the propagation of acoustic radiation from the model to the surrounding anechoic room. The test section has an open exit. The free jet from the test section exit then moves through an acoustically treated diffuser section, which leads to the primary fan, as shown in Fig. 2.

The fluctuating pressure is measured with two  $\frac{1}{2}$  inch (12.7 mm) ACO model 7046 free-field condenser microphones with linear output sensitivity of approximately 50 mV/Pa. The microphones are preamplified with an ACO  $\frac{1}{2}$  inch XLR model 412 preamp powered by a two-channel 200/28 V dc PS2900 power supply. The microphone signals are acquired simultaneously by a personal computer using a Microstar iDSC1816 A/D board. This board has onboard software-controlled anti-aliasing filters. The two microphones are positioned symmetrically on opposite sides of the cylinder at a radial distance of 0.61 m, as shown in Fig. 2. This location is well outside of the open jet. Measurements were made for several values of azimuthal angle,  $\varphi$ , as defined in Fig. 2.

Two circular cylinder models equipped with DBD plasma actuators were used in the current study. The first, which is shown

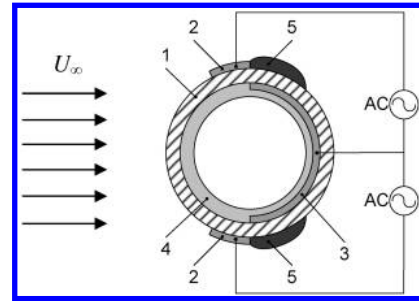


Fig. 3 Schematic of the cylinder model equipped with spanwise-oriented plasma actuators; 1: dielectric (quartz cylinder), 2: exposed electrode, 3: covered electrode, 4: Kapton tape, 5: plasma discharge.

schematically in Fig. 3, is equipped with two actuators with surface electrodes extending in the spanwise direction. The other, shown in Fig. 4, has PSVG actuators installed. These are formed from 15 streamwise-oriented surface electrodes, as shown in Fig. 4b. Both models are formed from identical quartz glass cylinders (labeled 1 in Figs. 3 and 4c) with an outer diameter  $D = 65$  mm, wall thickness  $d = 2.5$  mm, span of 533.4 mm and dielectric constant of 3.7. In both configurations, the cylinder wall serves as the dielectric barrier for the DBD plasma. The ends of both cylinder models terminate in plastic endplates, which elongate the models by 9.5 mm.

For the model with spanwise actuators shown in Fig. 3 the covered electrodes are common for both plasma actuators due to space limitations. These electrodes are made of Saint Gobain C661 1.6-mil-thick (0.041-mm-thick) copper foil tape with acrylic adhesive. As indicated, the outer, exposed electrode (label 2 in Figs. 3 and 4c) is mounted to the surface of the cylinder with its plasma-generating edges located at  $\pm 90^\circ$  with respect to the approach flow direction. This choice for the electrode positioning is based upon the idea that the best location for the plasma actuators is near the separation point [32,33]. The foil thickness is small compared with the boundary-layer thickness so that the presence of the exposed electrodes does not change the baseline flow significantly. The covered electrode (label 3) is mounted to the inner surface of the cylinder. Both inner and outer electrodes extend 0.457 m in the spanwise direction, encompassing 83% of the total span of the model.

For both actuators, eight layers of 5-mil-thick Kapton tape (label 4 in Figs. 3 and 4c) cover the inner electrodes and serve to prevent inner discharge. The inner and outer electrodes for the spanwise actuator have a small overlap, which gives rise to a large local electric field gradient. Plasma (label 5) forms near the edge of the exposed electrode and extends a distance along the cylinder's dielectric surface, as depicted in Fig. 3. As indicated in the figure, the actuators are connected to a high-voltage ac source (to be described).

For the streamwise plasma actuator model another configuration of electrodes is used, as shown in Fig. 4. It is designed to form PSVGs. A schematic illustration of the PSVG concept is shown in Fig. 4a. The multiple exposed electrodes with spanwise spacing,  $z$ , are aligned parallel to the flow streamlines. The covered electrode is common for all exposed electrodes so that the plasma discharge ignites at both edges of each exposed electrode. This arrangement creates opposing wall jets, which collide and give rise to pairs of counter-rotating vortices. In the cylinder application these will introduce streamwise vorticity into the nascent wake shear layers, increase cross-stream mixing and thereby reduce large-scale spanwise vortex shedding. In the current study, the cylinder model has 15 exposed streamwise-oriented electrodes of 0.25 in. (6.35 mm) width with a spanwise wavelength  $z = 1.25$  in. (31.75 mm). The PSVG actuators cover the windward half of the cylinder (from  $-90^\circ$  to  $+90^\circ$ ), as shown in Fig. 4c. The ends of the exposed electrodes are tied together at the rear side of the model. The covered electrode is similar to the one used for the spanwise model but it is located under the windward half of the cylinder. Photographs of both cylinder models in the wind-tunnel facility with the plasma discharge visible are presented in Fig. 5.

In this study, the spanwise actuator uses a positive sawtooth waveform with ac voltage of 55 kV peak-to-peak at 1000 Hz.

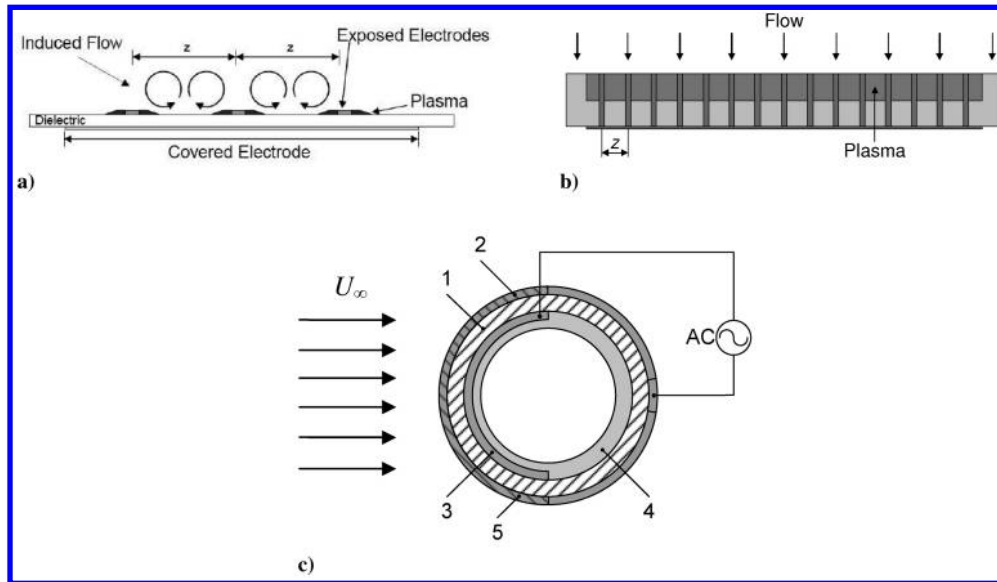


Fig. 4 a) Schematic illustration of PSVG actuator concept, b) top view of cylinder model with PSVG installed, c) cross-sectional view of cylinder showing a single streamwise-oriented actuator; 1: dielectric (quartz cylinder), 2: exposed electrode, 3: covered electrode, 4: Kapton tape, 5: plasma discharge.

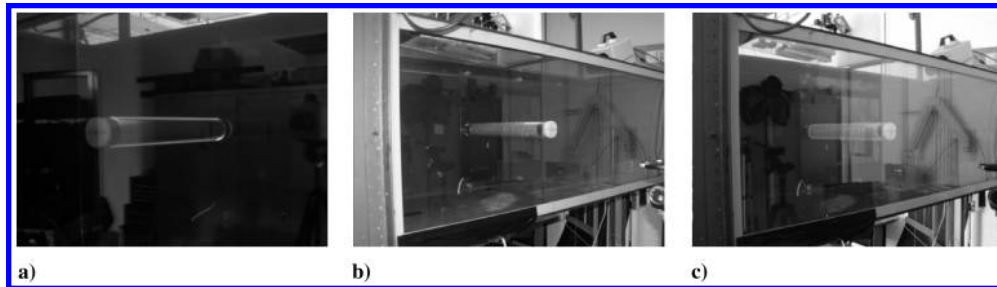


Fig. 5 Cylinder models with a) spanwise and PSVG actuators in the wind tunnel: b) off, and c) on.

The streamwise actuators use a sinusoidal ac voltage of 69 kV peak-to-peak at 500 Hz. While the sawtooth waveform has been shown to give a higher body force [19,21], the sinusoidal waveform is chosen for PSVG in order to reduce the load on the amplifier because of the high total electric capacitance of the series of 15 streamwise actuators. The high voltage is measured by a LeCroy PPE20kV dc high-voltage probe with a LeCroy LT262 oscilloscope.

The high-frequency, high-amplitude ac voltage is created using the circuit shown in Fig. 6. A low-amplitude signal from an arbitrary waveform function generator (e.g., Agilent Technologies model

33220A) is first supplied to two, two-channel power amplifiers (Crown XT4000). The amplified voltage from each of the four channels is then fed through a resistor module containing four  $2\ \Omega$ , 300 W ballast resistors that are connected together at the primary coils of two 1:360 transformers with a maximum output voltage of 25 kV ac (Corona Magnetics). The primary coils of the transformers are connected in parallel but in the opposite polarity. The low-potential leading-out wires of the secondary coils are connected to ground. High voltage required by the plasma actuator is taken from the two high-potential leads of the transformers giving the same signal in the opposite polarity so that the effective winding ratio of this system is 1:720.

A dielectric barrier discharge is accompanied by high-intensity radio frequency electromagnetic noise. An antinoise filter is used to suppress this noise. In essence, it is a low-pass filter of  $O(10\text{ MHz})$  cutoff consisting of two inductors (eight turns, ferrite core, 31.1 mm OD, 19.1 mm ID, 15.9 mm height) and a battery of four high-voltage capacitors (25 pF, 15 kV dc max). The filter does not affect the actuation frequency but prevents high-frequency noise originating from microdischarges from entering the high-voltage wires that feed the plasma actuators. For typical laboratory experiments, these wires are relatively long and radiate electromagnetic waves like an antenna if the filter is not installed.

#### IV. Flow Control Experiments

This section presents the results from a series of flow control experiments using DBD plasma actuators mounted on the two circular cylinder models shown in Figs. 3 and 4. Measurements presented include global flow visualization and near-wake LDA mean velocity and turbulence intensity velocity profiles. The Reynolds number for the LDA wake measurements (based on

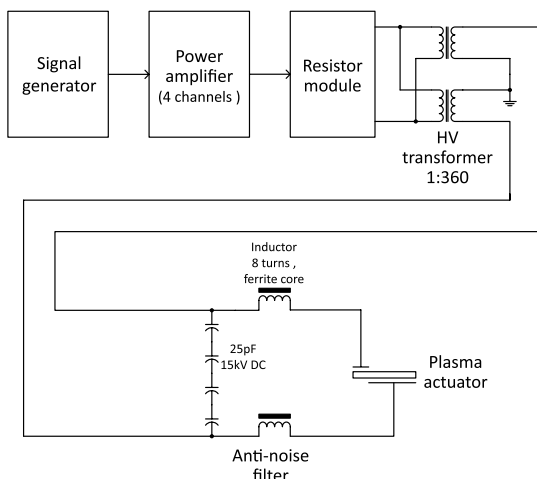


Fig. 6 Plasma-generation circuit and antinoise filter used in the experiments.

freestream velocity and cylinder diameter) is  $Re_D = 85,000$  (with a freestream speed  $U_\infty = 20 \pm 1$  m/s). To facilitate effective flow visualization and thereby clearly illustrate the modes of flow control, the Reynolds number was reduced for the visualization images presented in this paper to  $Re_D = 17,000$ . In each case, measurements were performed both with and without plasma actuation.

In a previous flow control study [22,23] two actuation strategies were used and found to be effective: quasi-steady plasma-induced blowing and unsteady or pulsed plasma actuation. In the unsteady mode the high-frequency ac signal was modulated at a lower frequency related to a characteristic time scale of the flow. Optimum results corresponded to  $St_D = 1$ . One major focus of the current study was to compare the performance of PSVG with actuators using spanwise electrodes. PSVGs are operated only in quasi-steady mode. Hence, both spanwise and PSVG plasma actuators in the current study were always operated in a quasi-steady mode in the sense that an unmodulated ac carrier of constant frequency was used.

The power input to the actuators in these experiments was modest. For spanwise plasma actuation, the total input power to the two actuators in their quasi-steady mode of operation was measured to be 140 W or 306 W/m. For the 15 electrodes that comprised the PSVG, the total power input was measured to be 550 W or 962 W/m span.

### A. Flow Visualization Results

The influence of the plasma actuators on the global structure of the cylinder flow is presented first. Flow visualization videos were acquired from the high-speed camera operated at a frame rate of 250 frames per second. Representative sample images from the high-speed video were extracted and are presented in this section.

An image of the flow over the cylinder with the spanwise actuators off is shown in Fig. 7. The flow obviously undergoes subcritical separation leading to a large separated flow region that is accompanied by unsteady, Kármán vortex shedding at a Strouhal number of  $St_D = 0.19$ , i.e., approximately  $f_s = 58$  Hz for  $Re_D = 85,000$ . The corresponding flow with spanwise plasma actuators operating in quasi-steady mode is also shown for comparison in Fig. 7. This figure shows that the two wall jets produced by the plasma actuation significantly delay boundary-layer separation and reduce the size of the separated flow region. Note that the boundary-layer separation location has moved to the aft section of the cylinder surface. The global wake structure is dramatically altered, and it is apparent that Kármán vortex shedding has been suppressed. Comparison of the baseline and plasma flow control images shown in Fig. 7 nicely illustrates the so-called plasma-fairing effect by which the cylinder

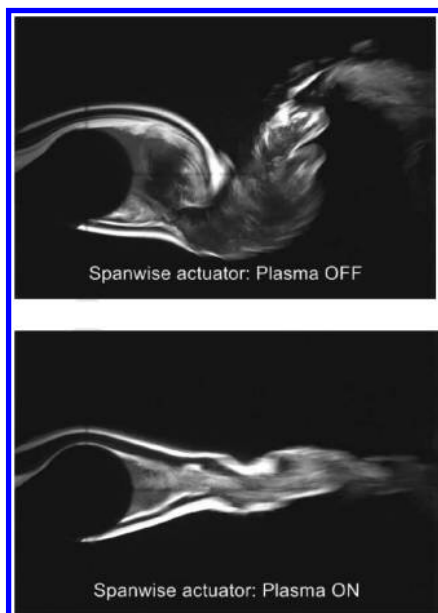


Fig. 7 Near-wake flow visualization of the baseline cylinder flow and with spanwise plasma actuation ( $Re_D = 17,000$ ).

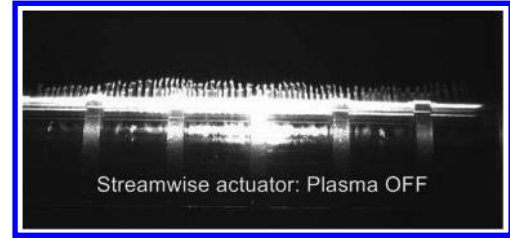


Fig. 8 Near-wake flow visualization image with PSVG off ( $Re_D = 17,000$ ). Image plane is normal to the oncoming flow.

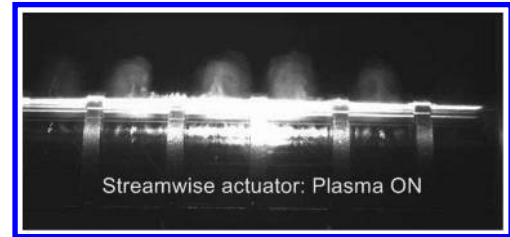


Fig. 9 Near-wake flow visualization image with PSVG on ( $Re_D = 17,000$ ). Image plane is normal to the oncoming flow.

has been effectively streamlined by plasma flow control. This effect has been demonstrated at subcritical  $Re_D$  in excess of  $10^5$ , considerably higher than reported in [22].

To visualize the effect of the PSVG, a miniature video camera was mounted inside the wind tunnel, downstream of the cylinder model and facing the upstream direction. The laser light sheet extends in the spanwise direction and was oriented normal to the oncoming flow. The location coincides with the cylinder axis at  $x = 0$ . The image plane lies directly above the cylinder model. Figure 8 shows a sample flow visualization image obtained with the PSVG off. Individual smoke streaklines injected via a rake at the tunnel inlet are visible and these serve to mark the free shear layer that results from subcritical flow separation from the cylinder model. Although not apparent from the static image shown in Fig. 8, high-speed flow visualization video shows the oscillation of the streaklines normal to the cylinder surface at the Kármán shedding frequency. This is a consequence of the formation of large-scale Kármán vortices downstream of the image plane. Also visible in Fig. 8 are several streamwise-oriented electrodes on the cylinder surface that collectively form the PSVG.

Figure 9 presents a flow visualization image obtained with the cylinder PSVGs on. Spanwise counter-directed plasma-induced wall

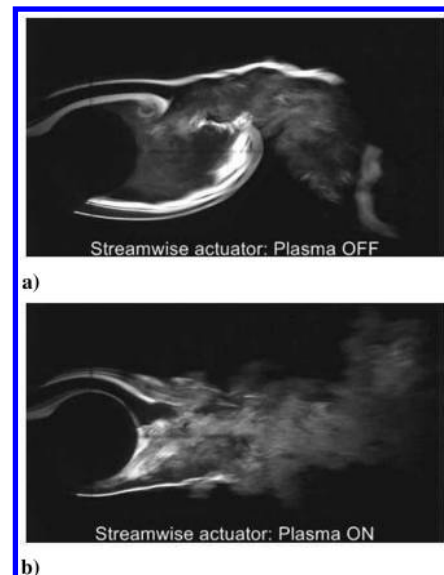


Fig. 10 Near-wake flow visualization comparison showing the effect of PSVG.



jets (see Fig. 4a) are shown to interact to form pairs of counter-rotating discrete streamwise vortices that are clearly visible in the image. These serve to introduce streamwise vorticity into the nascent wake shear layers, which forms the basis for flow control.

Figure 10 compares near-wake flow visualization images obtained with the PSVGs off and on. This figure shows that the introduction of streamwise vorticity into the cylinder wake delays flow separation from the cylinder, and as a consequence, large-scale Kármán shedding associated with the global instability of the wake flow is again clearly suppressed. Comparison of the image with spanwise plasma actuation shown previously in Fig. 7 and the PSVG case shown in Fig. 10 suggests that the cylinder wake with PSVG contains a higher level of smaller-scale vorticity and there is apparently intensive cross-stream mixing. The resulting wake width is greater for the PSVG case. These aspects will be addressed further in the next section, which presents near-wake LDA measurements with both types of plasma flow control.

The flow visualization results presented here are consistent with the turbulent boundary-layer plasma flow control mechanisms identified by Schatzman and Thomas [31]. For the spanwise-oriented actuators the mechanism is based mainly on the creation of quasi-steady plasma-induced wall jets that adhere to the cylinder surface via a Coanda effect. These serve to add momentum to the near-wall boundary layer keeping the flow attached to the cylinder surface. In contrast, the streamwise plasma actuators work as streamwise vortex generators, which create relatively large-scale streamwise vorticity. This promotes cross-stream momentum exchange between the outer flow and near-wall regions and thereby delays flow separation from the cylinder. In both cases, delaying separation has the effect of suppressing Kármán vortex shedding.

## B. LDA Wake Measurements

### 1. Spanwise-Oriented Plasma Actuators

In this section, representative results from a series of LDA measurements obtained at  $Re_D = 85,000$  are presented that serve to quantify the effect of both spanwise and PSVG plasma actuators on the cylinder near wake. It should first be noted that the charge on the olive oil droplets used for LDA seeding is, at most, a few hundred electrons and is associated with their shear-dominated formation process in the seeder. Dimensional analysis confirms that even for the highest electric field encountered in these experiments, aerodynamic forces on the droplets are several orders of magnitude greater than the electrostatic force. Consistent with this, none of the LDA measurements suggest that seed particles follow electric field lines (which have been computed in the course of complementary numerical simulations [23]).

Figure 11 compares cross-stream profiles of streamwise-component turbulence intensity for the natural cylinder near wake with those for plasma flow control using the twin spanwise-oriented plasma actuators. Measurements are presented for representative locations  $x/D = 1, 2, 4$  and  $8$ , where  $x/D$  is the ratio of the streamwise spatial coordinate, measured from the cylinder axis, to the cylinder diameter. At  $x/D = 1$ , the plasma actuation has the effect of reducing the streamwise fluctuation intensity in the wake shear layers by approximately 30%. Reduced turbulence levels for the plasma-on case also occur at  $x/D = 2$  except at the wake centerline where the intensity levels are comparable. At  $x/D = 4$  the intensity levels in the plasma-on case are reduced across the wake by approximately 40% from corresponding values in the natural wake. This figure also clearly demonstrates that the time-mean wake width is considerably reduced under the influence of plasma actuation,

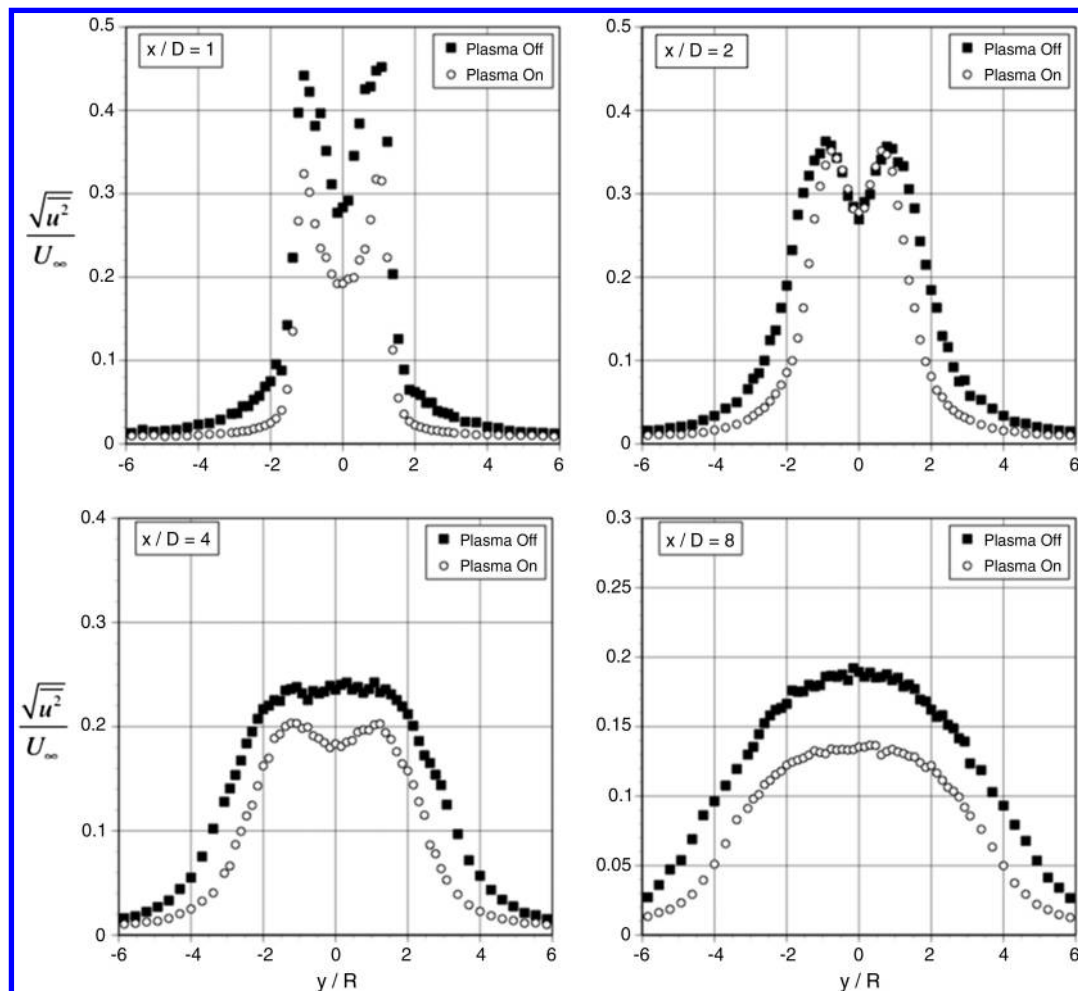


Fig. 11 Comparison of streamwise-component turbulence intensity cross-stream profiles in the cylinder near wake for the model with spanwise-oriented plasma actuators at several streamwise locations.

consistent with the flow visualization results (at lower  $Re_D$ ) shown previously. That the effect of plasma actuation on the cylinder wake is sustained is apparent from comparison of the streamwise intensity profiles at  $x/D = 8$ , which show significant reduction in  $u$ -component turbulence levels across the wake for the plasma-on case. For example, at the wake centerline the streamwise-component intensity is reduced by 32% due to plasma actuation. The lower  $u$ -component fluctuation levels are associated with the elimination of large-scale vorticity in the cylinder wake as shown previously in the flow visualization images.

Figure 12 presents corresponding profiles of the lateral (cross-stream)  $v$ -component fluctuation intensity both with and without spanwise plasma actuation. Note that values of  $\sqrt{v^2}/U_\infty$  in the natural wake are quite high in comparison with the streamwise component and this is associated with the unsteady lateral motion of the near wake due to large-scale Kármán vortex shedding. That is, they are not true turbulence levels per se, but rather an indicator of a very unsteady lateral flow associated with Kármán vortex shedding. Consistent with previously presented flow visualization, which showed near elimination of Kármán shedding by the spanwise plasma actuators, the spanwise actuator-on lateral intensity results at  $x/D = 1$  exhibit a 53% reduction in  $\sqrt{v^2}/U_\infty$  from the natural flow level. Reductions at  $x/D = 2$  and 4 are also apparent at approximately 32% and 21%, respectively. This is sustained farther downstream at  $x/D = 8$  where the centerline values are still approximately 25% lower than the natural case. Collectively, these values suggest a significant plasma-induced suppression of unsteady lateral wake motion associated with near-wake Kármán vortex shedding. This is

also manifest in the observation from both Fig. 11 and 12 that the time-average near-wake width (as defined by the fluctuation intensity profiles) is thinner in the plasma-on cases; for example 16% thinner at  $x/D = 8$ .

Figure 13 compares the near-wake mean velocity profiles at selected representative streamwise locations for the natural baseline flow and for plasma actuation with spanwise-oriented electrodes. It is interesting to note that the mean wake defect is actually greater but the wake thinner for the case of spanwise plasma actuation at  $x/D = 2$ . This is a manifestation of the suppression of Kármán vortex shedding, which reduces the cross-stream oscillation of the near wake and spatially localizes the wake velocity defect. This has the effect of rendering the time-mean wake defect larger and thinner for streamwise locations near the cylinder. Figure 13 shows a gradual transition with increased  $x/D$  such that the mean wake defect for the case of spanwise plasma actuation becomes smaller than the baseline; for example it is approximately 45% of the baseline maximum defect by  $x/D = 8$ .

## 2. PSVG Plasma Actuation

Figure 14 compares profiles of streamwise fluctuating component intensity for both the natural cylinder wake and for the case with PSVG flow control. Unlike the spanwise plasma actuation case, use of the PSVG does not give rise to large reduction in  $u$ -component intensity in the wake shear layer at  $x/D = 1$  and, in fact, leads to an increase near the center of the wake at  $x/D = 2$ . This is due to the fact that the PSVG serves to inject streamwise vorticity into the nascent wake shear layer, which promotes cross-stream mixing and

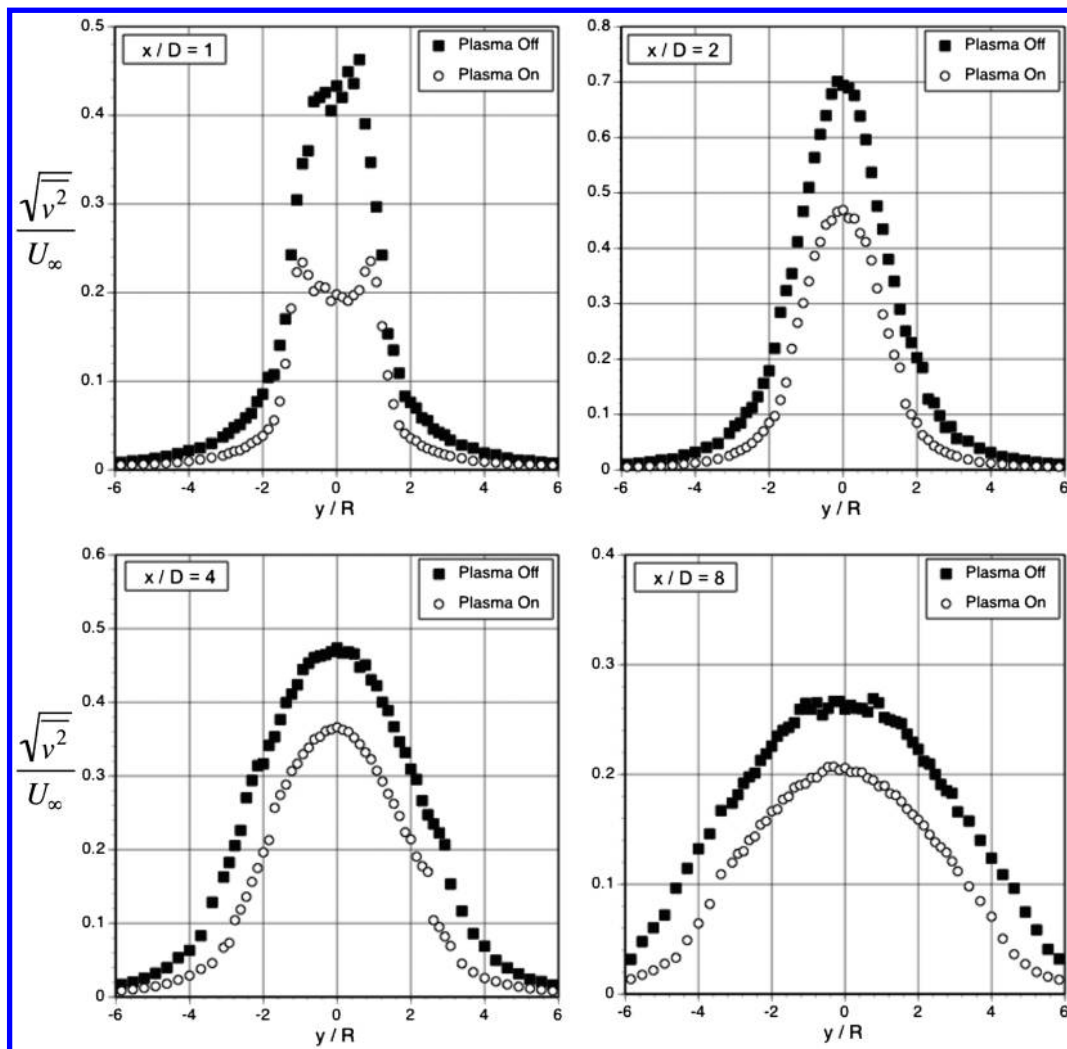


Fig. 12 Comparison of lateral-component turbulence intensity profiles in the cylinder near wake for the model with spanwise-oriented plasma actuators.

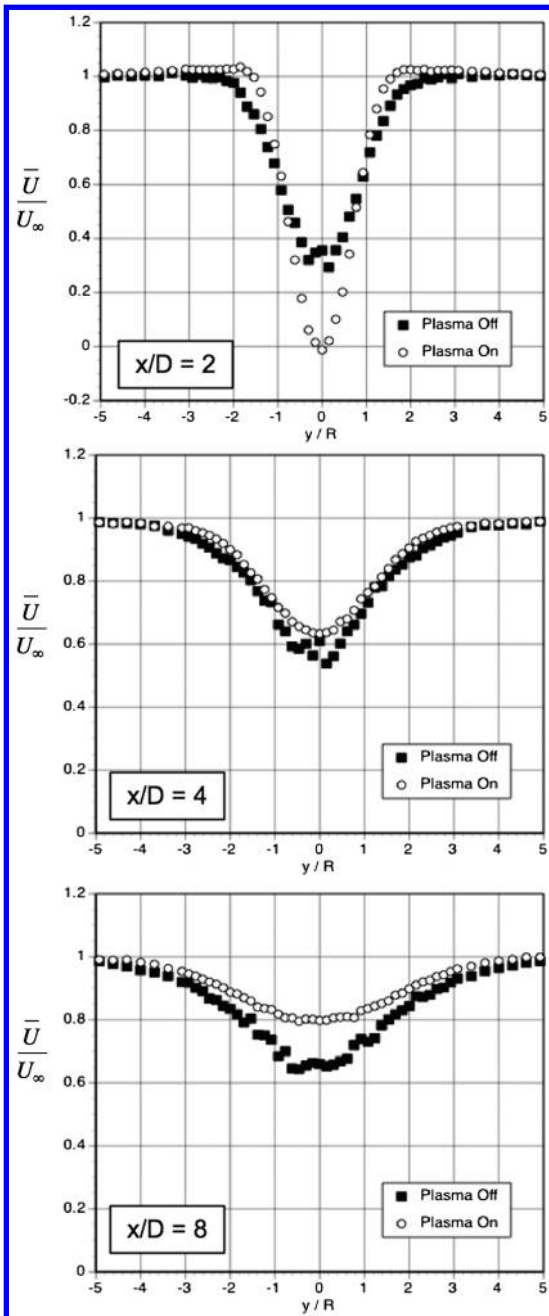


Fig. 13 Wake mean velocity profiles for natural and spanwise-oriented plasma actuation cases.

increased turbulence levels in the central portion of the wake. It will be shown that flow separation from the cylinder is delayed, which reduces wake unsteadiness associated with the Kármán shedding. Consequently, streamwise-component intensities obtained farther downstream are lower than baseline for the PSVG case, as shown in Fig. 14. In fact, comparison of  $\sqrt{u^2}/U_\infty$  profiles for spanwise and PSVG plasma-on cases at  $x/D = 8$  actually reveal lower levels for the PSVG flow control.

The influence of the PSVG flow control in reducing unsteadiness associated with Kármán shedding is perhaps most apparent from examination of lateral-component turbulence intensity measurements,  $\sqrt{v^2}/U_\infty$ , shown in Fig. 15. At  $x/D = 1$  the lateral intensity with the PSVG turned on is higher than was the case for spanwise plasma actuation. However, PSVG still gives rise to considerably lower  $v$ -component fluctuation levels relative to the baseline case. By  $x/D = 2$  and 4, the reduction in lateral velocity fluctuations associated with Kármán shedding is comparable to that achieved by

using the twin spanwise actuators and is even lower at the  $x/D = 8$  location.

It should be noted that the LDA traverses for the PSVG shown in Figs. 14 and 15 were obtained at a spanwise location aligned with one of the exposed electrodes. Cross-stream LDA profiles were also obtained at a spanwise location centered between adjacent electrodes and no significant differences were noted. A representative comparison is made in Fig. 16. In particular, this figure compares streamwise- and lateral-component intensity profiles obtained at  $x/D = 1$  for PSVG actuation at spanwise locations both directly over and centered between exposed electrodes. Within experimental uncertainty, the measurements show no significant differences. This implies that the vortex induced cross-stream mixing is very rapid such that by the first streamwise measurement location ( $x/D = 1$ ) the wake flow is already spanwise uniform in the time-mean sense. This rapid tendency toward spanwise homogeneity in the mean has been confirmed in additional LDA surveys over fine mesh rectangular measurement grids for  $x/D < 1$  (not presented here).

Figure 17 compares cross-stream profiles of the ratio  $\sqrt{u^2}/\sqrt{v^2}$  in the cylinder wake at  $x/D = 8$  for cases involving the PSVG and spanwise plasma actuation on the upstream cylinder. There is a clear and sustained difference associated with the type of plasma actuation; the wake with the PSVG actuation exhibits consistently larger values than those with spanwise actuation. This suggests a more highly mixed, less anisotropic wake structure associated with the injection of streamwise vorticity near the cylinder.

Figure 18 compares the near-wake mean velocity profiles at selected representative streamwise locations for the natural baseline flow and for PSVG plasma actuation. As was the case for spanwise actuation, the wake defect for PSVG is larger than the baseline for  $x/D = 2$ . This is a consequence of the elimination of lateral near-wake oscillation due to Kármán shedding. Farther downstream, the wake defect for PSVG is reduced relative to the baseline and the mean wake width is also reduced. Reduction in mean wake defect with PSVG flow control is comparable to that achieved with plasma actuation with spanwise-oriented electrodes.

## V. Near-Field Pressure Fluctuations

In this section, microphone measurements that demonstrate effective plasma-induced suppression of pressure fluctuations associated with Kármán vortex shedding are presented. The fluctuating pressure measured by the microphones contains contributions from both the cylinder wake and noise produced by the anechoic wind-tunnel facility. For this reason, the objective of the microphone measurements reported in this study is to document *changes* in the pressure spectrum that result from operation of the plasma actuators. The sound pressure power spectral density plots for both cylinder models are presented in Fig. 19. They were obtained at the same Reynolds number as the previously presented LDA measurements;  $Re_D = 85,000$  (corresponding to a freestream speed of  $U_\infty = 20$  m/s). The data are plotted in dB units based on the reference pressure of  $20 \mu\text{Pa}$  and the reference bandwidth of 1 Hz. Five cases are shown: 1) wind-tunnel background noise without the model; 2) no plasma actuation, spanwise actuator; 3) steady plasma actuation, spanwise actuator; 4) no plasma actuation, PSVG actuator; and 5) steady plasma actuation, PSVG actuator.

Pressure fluctuations at the Kármán vortex shedding frequency are apparent in the form of a dominant spectral peak in the no-actuation spectra (i.e., the plasma-off cases). In the plasma-on case, this spectral peak is almost completely suppressed by the PSVG. For the case involving twin spanwise actuators, a much lower amplitude peak at higher frequency is observed. The shift to higher frequency is likely associated with a reduction in the spatial extent of the separated flow region,  $\ell_s$ . That is, for shedding at constant Strouhal number, the shedding frequency,  $f_s \propto U_\infty/\ell_s$ , suggesting a shift to higher shedding frequency as the extent of the separated flow region  $\ell_s$  is reduced. Reduction in the extent of the separated flow region with plasma actuation (at considerably lower  $Re_D$ ) is quite apparent in the flow visualization image shown in Fig. 7.



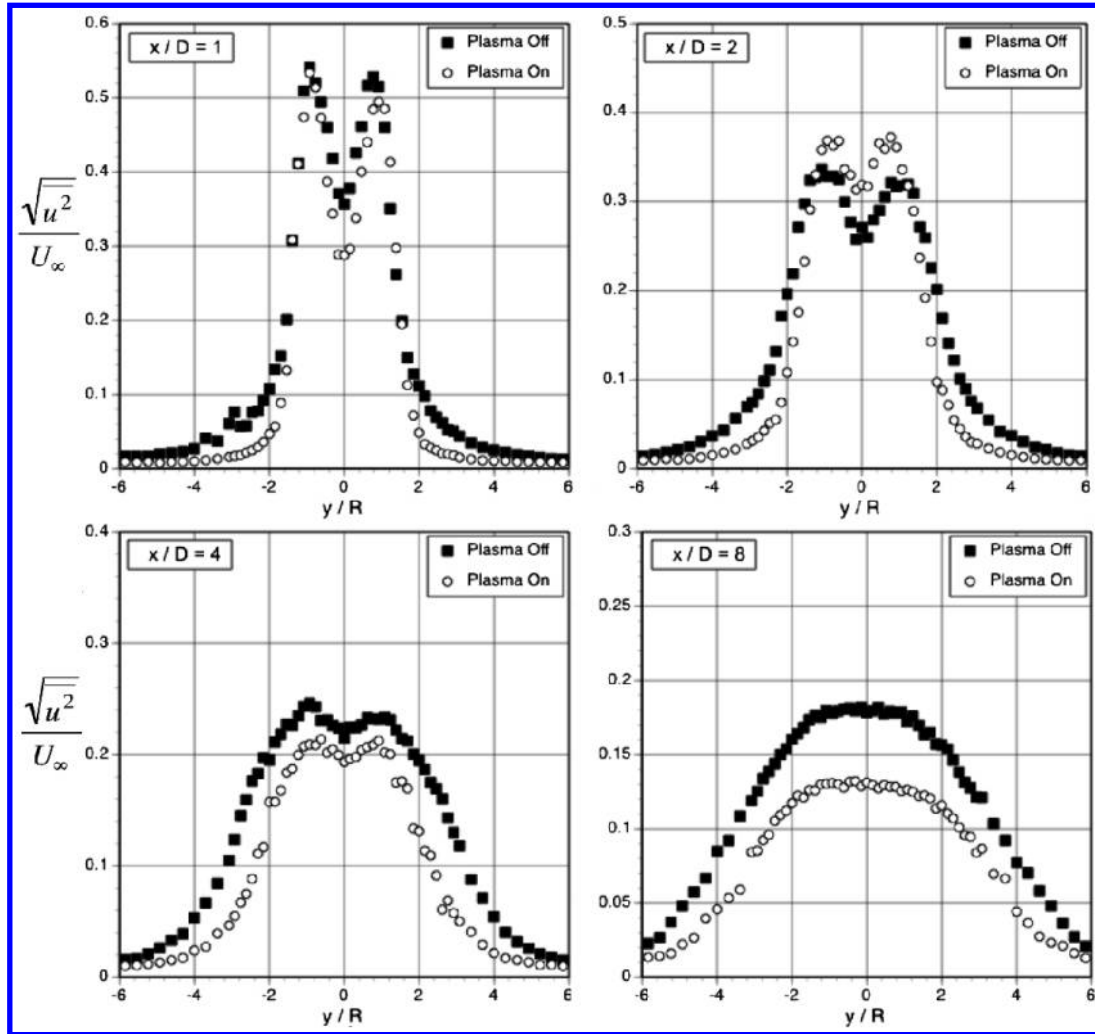


Fig. 14 Comparison of streamwise-component turbulence intensity profiles in the cylinder near wake for the model with PSVG plasma actuators.

The main source of the acoustic radiation in a flow around a bluff body at low Mach numbers is a dipole source associated with large pressure fluctuations at the body surface due to unsteady vortex shedding. The contribution from other sources of noise like the wake turbulence noise or separated boundary-layer noise is very small in comparison to that dipole source. The power spectral density of the fluctuating pressure signal was integrated numerically from 40 to 70 Hz to obtain the change in fluctuating pressure level associated with the suppression of Kármán wake vortices. Calculations show that the near-field fluctuating pressure level is reduced by the plasma actuation by 11.2 dB for the spanwise actuator case and by 14.2 dB for the PSVG actuator.

In addition to the suppression of vortex shedding, the actuator creates its own tonal noise, due to the unsteady body force and air thermal expansion associated with the (small) heat dissipation in the discharge. This noise can be seen in Fig. 19 as multiple narrowband peaks associated with the actuation frequency (either 500 or 1000 Hz) and its harmonics. To estimate the contribution of the plasma actuator noise, the difference between the sound pressure level of the Kármán shedding spike (from 40 to 70 Hz) and the actuation frequency spikes (1, 2, 3, and 4 kHz for the spanwise actuator and 500 Hz, 1, 1.5, 2, 2.5, 3, 3.5, and 4 kHz for the PSVG) was calculated. This difference equals 11.6 dB for the spanwise actuator and 7.0 dB for streamwise actuator. Thus, we can conclude that the actuator-induced noise is not significant compared with the gains achieved by suppressing the Kármán shedding peak. For the integration of the whole frequency range from 40 to 4 kHz, which includes the actuator-induced noise and the wind-tunnel noise, the pressure fluctuations are reduced by 8.0 and 5.9 dB for spanwise

actuator and PSVG, respectively. The spanwise model exhibits a better result because it has lower actuator-induced noise. Although not considered in the design of the flow control experiments reported in this paper, the ac carrier frequency used for the DBD plasma actuation could be set sufficiently high so as to be above the threshold of human hearing, thereby fully negating the contribution of the plasma actuator to the acoustic field. In fact, as shown in Fig. 7 of the paper by Thomas et al. [21], at fixed applied voltage the plasma-induced body force actually increases with increased ac frequency.

Figures 20 and 21 present representative linear coherence and phase spectrum measurements obtained in the anechoic wind tunnel for the cylinder models using spanwise plasma actuators and PSVG, respectively. In each case the linear coherence and phase spectrum was obtained with two symmetrically placed microphones located at  $\varphi = 0^\circ$  (see Fig. 2). Each microphone was situated 9.4 diameters from the cylinder. In both figures the plasma-off case exhibits peak linear coherence values near unity for the shedding frequency,  $St_D = 0.19$ . The corresponding phase spectrum shows that the pressure fluctuations are  $\pi$  radians out of phase, which is consistent with a dipole source associated with Kármán vortex shedding from the cylinder. When plasma actuation is applied, both Figs. 20 and 21 show a reduction in linear coherence at  $St_D = 0.19$ . Corresponding phase spectra show that the pressure fluctuations remain antisymmetric over a frequency band centered on  $St_D = 0.19$ . Thus, with plasma actuation, the pressure fluctuations emanating from the wake remain fundamentally antisymmetric but at dramatically reduced amplitude, as shown in the autospectra of Fig. 19.

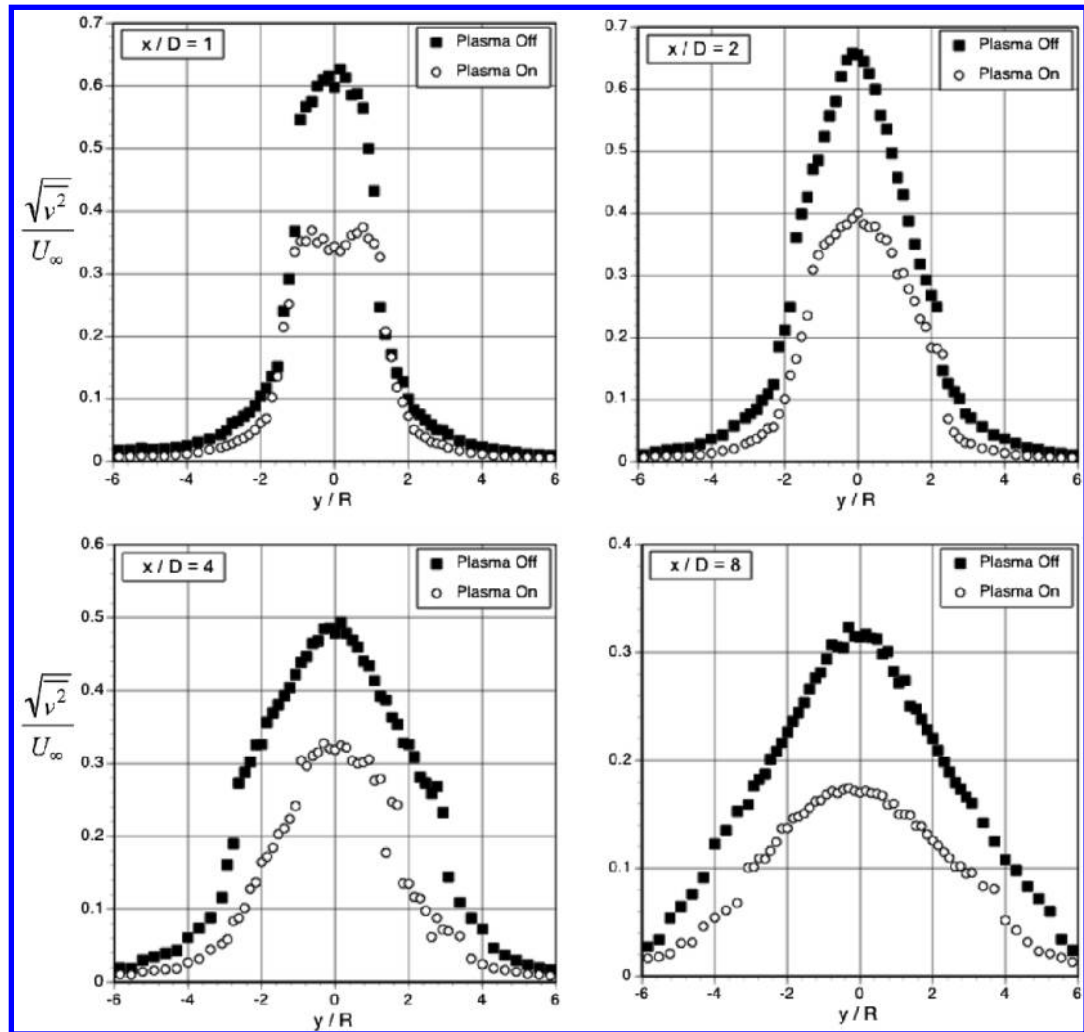


Fig. 15 Comparison of lateral-component turbulence intensity profiles in the cylinder near wake for the model with PSVG plasma actuators.

## VI. Conclusions

The results of the flow control experiments presented in this paper clearly demonstrate the feasibility of the plasma-fairing concept for the effective streamlining of bluff-body flows at high subcritical Reynolds number. In particular, it is demonstrated that surface-mounted DBD plasma actuators that are oriented in the spanwise direction delay boundary-layer flow separation and thereby effectively streamline the circular cylinder in crossflow. The operation of the actuators is shown to effectively suppress Kármán vortex

shedding. As a consequence, turbulence levels in the wake are significantly reduced, as is the wake width and mean velocity defect. The results presented in this paper were obtained at  $Re_D = 85,000$  but it should be noted that similar flow control results have been obtained for  $Re_D > 10^5$ .

The streamwise-oriented PSVG actuators also showed an effective control authority by producing counter-rotating vortices within the nascent wake shear layers. This has the effect of creating cross-stream momentum transfer, which also delays flow separation from

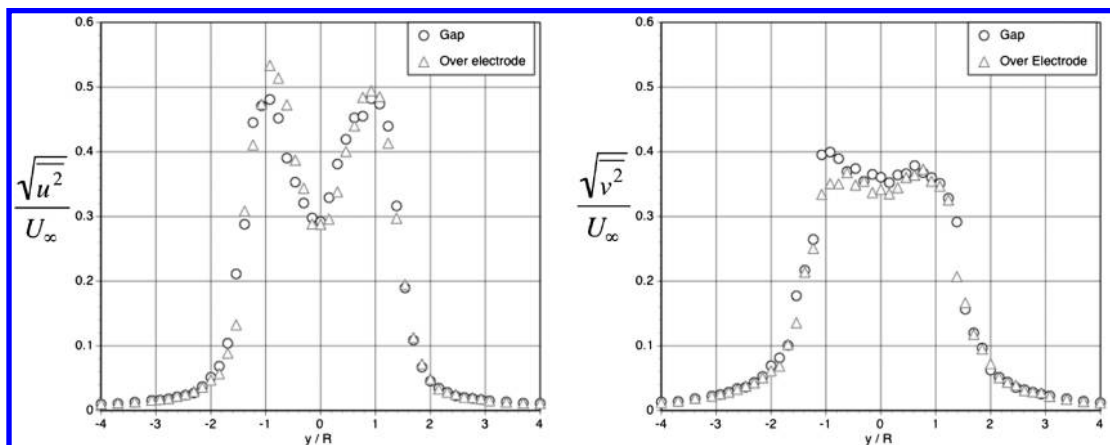


Fig. 16 Comparison of streamwise- and lateral-component fluctuation intensity profiles at  $x/D = 1$  with PSVG for spanwise locations over an electrode and centered on the interelectrode gap.

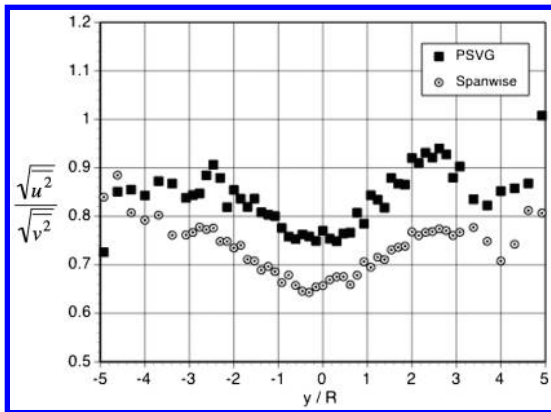


Fig. 17 Comparison of  $\sqrt{u'^2}/\sqrt{v'^2}$  at  $x/D = 8$  for PSVG and spanwise-oriented plasma actuators.

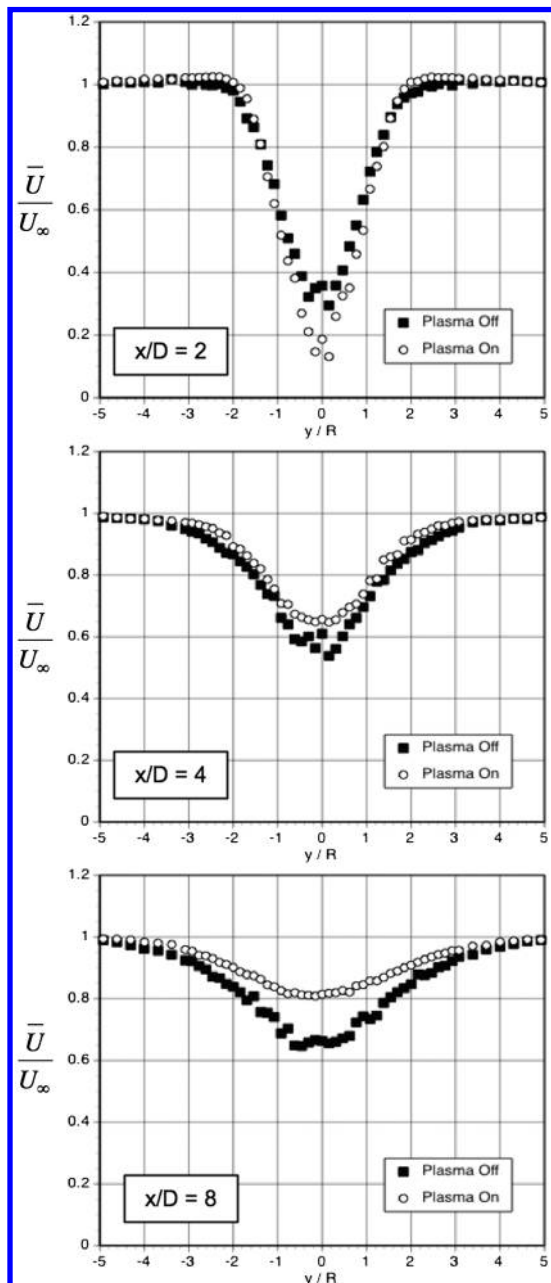


Fig. 18 Wake mean velocity profiles for natural and PSVG plasma actuator cases.

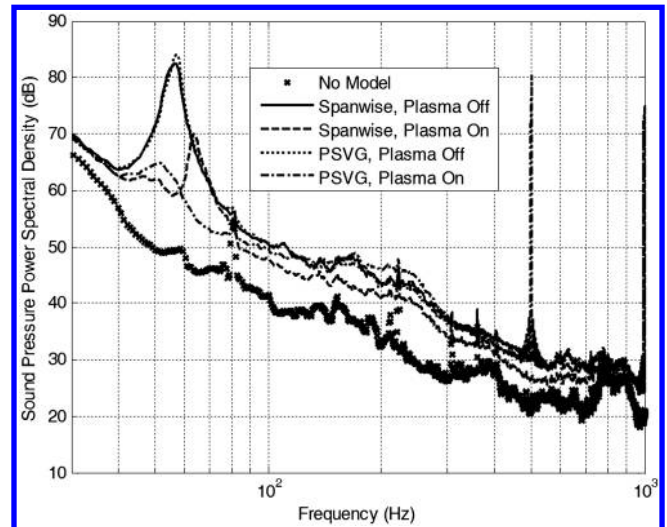


Fig. 19 Effect of plasma actuation on sound pressure level spectra ( $Re_D = 85,000$ ).

the cylinder surface. As a consequence, the Kármán shedding is again strongly suppressed, although the underlying mechanism is quite different than for the spanwise plasma actuators. For both spanwise and PSVG plasma actuation, the cylinder near wake becomes more benign as evidenced by a dramatic reduction in the lateral fluctuating velocity component associated with suppression of large-scale vortex shedding.

As expected, the reduction in large-scale vortex shedding has a favorable effect in reducing near-field pressure fluctuations. Microphone measurements in an anechoic wind tunnel confirm the reduction of near-field pressure fluctuations associated with the reduction of vortex shedding. For spanwise and PSVG actuation, near-field pressure levels are reduced by 11.2 and 14.2 dB, respectively, in a frequency band centered on the shedding frequency. Since plasma actuation is associated with an unsteady body force and thermal expansion during the high-voltage ac cycle, it produces acoustic tones at the actuation frequency and its harmonics. However, these tones are found to be 8.0 and 5.9 dB less than Kármán shedding noise from the cylinder. In the experiments reported here, it

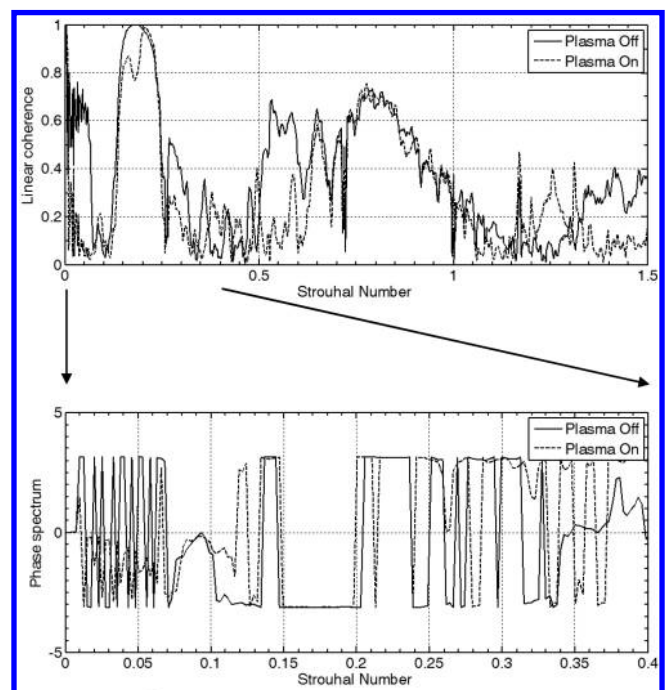
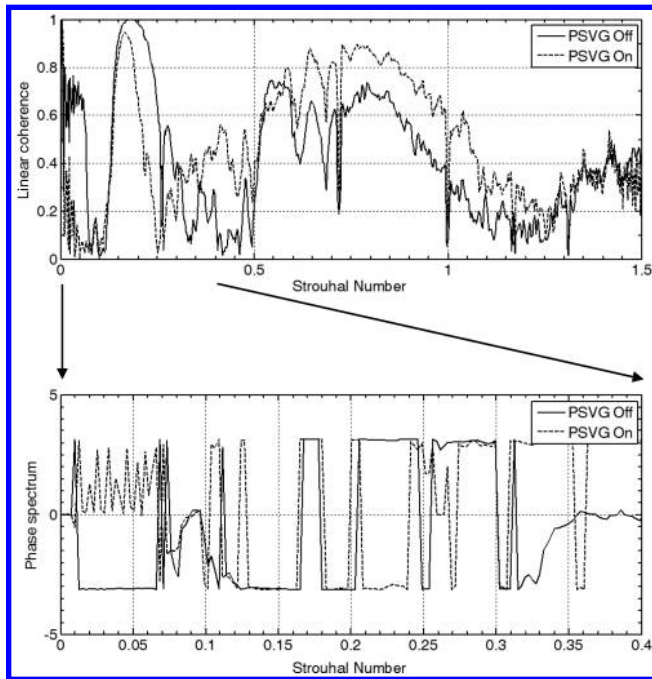


Fig. 20 Linear coherence and phase spectrum based on two-point microphone measurement for spanwise-oriented plasma actuators.





**Fig. 21 Linear coherence and phase spectrum based on two-point microphone measurement for PSVG plasma actuators.**

was found a net overall sound pressure level reduction of approximately 6–8 dB was achieved despite the presence of wind-tunnel noise and the plasma actuator noise. We consider these achievements to be encouraging, with regard to the use of plasma actuators in aeroacoustic control applications. Further, in actual applications the plasma ac excitation voltage could be applied at a carrier frequency above the threshold of human hearing rendering actuator noise irrelevant.

In reality, landing gear noise is not tonal in nature but is broadband due to the formation of multiple wakes from upstream gear elements that undergo unsteady interactions with downstream gear components. However, the ability demonstrated in this paper to reduce bluff-body wake unsteadiness by plasma actuation should prove useful in the control of these wake interactions with downstream components. A future focus is to apply the bluff-body plasma flow control techniques developed in this paper to a tandem-cylinder configuration with the goal of reducing unsteady surface pressure fluctuations associated with unsteady wake impingement on the downstream cylinder. The tandem-cylinder arrangement is viewed as another relevant geometry for aircraft landing gear. Subsequently, it is planned that this plasma-fairing technology will be applied to more realistic landing gear geometries.

### Acknowledgments

This work was supported by NASA under NRA NNX07AO09A monitored by Clif Horne and William Humphreys. This support is gratefully acknowledged.

### References

- [1] Siller, H., Drescher, M., Saueressig, G., and Lange, R., "Flyover source localization on a Boeing 747-400," Berlin Beamforming Conf., Paper BeBeC-2010-13, Feb. 24–25 2010.
- [2] Guérin, S., and Siller, H., "A hybrid time-frequency approach for the noise localization analysis of aircraft fly-overs," 14th AIAA/CEAS Aeroacoustics Conf., AIAA Paper 2008-2955, 2008.
- [3] Michel, U., Barsikow, B., and Haverich, B., "Investigation of airframe and jet noise in high-speed flight with a microphone array," 3rd AIAA/CEAS Aeroacoustics Conf., Atlanta, AIAA Paper 1997-1596, 1997.
- [4] Guérin, S., Michel, U., Siller, H., Finke, U., and Saueressig, G., "Airbus A319 Database from Dedicated Flyover Measurements to Investigate Noise Abatement Procedures," 11th AIAA/CEAS Aeroacoustics Conf., AIAA Paper 2005-2981, Monterey, CA, 2005.

- [5] Guérin, S., Michel, U., Siller, H., Finke, U., and Saueressig, G., "Airbus A319 Database from Dedicated Flyover Measurements to Investigate Noise Abatement Procedures," 11th AIAA/CEAS Aeroacoustics Conf., AIAA Paper 2005-2981, Monterey, CA, 2005.
- [6] Heller, H. H., and Dobrzynski, W. M., "Unsteady Surface Pressure Characterization of Aircraft Components and Far-Field Radiated Airframe Noise," *Journal of Aircraft*, Vol. 15, No. 12, 1978, pp. 809–815.  
doi:10.2514/3.58453
- [7] Dobrzynski, W., Chow, L. C., Guion, P., and Shiells, D., "A European Study on Landing Gear Airframe Noise Sources," 6th AIAA/CEAS Aeroacoustics Conf. & Exhibit, AIAA Paper 2000-1971, Lahaina, HI, June 2000.
- [8] Dobrzynski, W., Chow, L. C., Guion, P., and Shiells, D., "Research into Landing Gear Airframe Noise Reduction," 8th AIAA/CEAS Aeroacoustics Conf. & Exhibit, AIAA Paper 2002-2409, Breckenridge, CO, 2002.
- [9] Guo, Y., "A Component-Based Model for Aircraft Landing Gear Noise," *Journal of Sound and Vibration*, Vol. 312, Nos. 4–5, 2008, pp. 801–820.  
doi:10.1016/j.jsv.2007.11.013
- [10] Guo, Y., "A Statistical Model for Landing Gear Noise Prediction," *Journal of Sound and Vibration*, Vol. 282, Nos. 1–2, 2005, pp. 61–87.  
doi:10.1016/j.jsv.2004.02.021
- [11] Li, F., Khorrami, M. R., and Malik, M. R., "Unsteady Simulation of a Landing-Gear Flow Field," AIAA Paper 2002-2411, 2002.
- [12] Jenkins, L. N., Khorrami, M. R., Choudhari, M. M., and McGinley, C. B., "Characterization of Unsteady Flow Structure Around Tandem Cylinders for Component Studies in Airframe Noise," 11th AIAA/CEAS Aeroacoustics Conf., AIAA Paper 2005-2812, Monterey, CA, May 2005.
- [13] Jenkins, L. N., Neuhart, D. H., McGinley, C. B., Choudhari, M. M., and Khorrami, M. R., "Measurements of Unsteady Wake Interference Between Tandem Cylinders," AIAA Paper 2006-3202, 2006.
- [14] Khorrami, M. R., Choudhari, M. M., Jenkins, L. N., and McGinley, C. B., "Unsteady Flowfield Around Tandem Cylinders as Prototype for Component Interaction Airframe Noise," 11th AIAA/CEAS Aeroacoustics Conf., Monterey, CA, AIAA Paper 2005-2866, May 2005.
- [15] Neuhart, D. H., Jenkins, L. N., Choudhari, M. M., and Khorrami, M., "Measurements of the Flowfield Interaction Between Tandem Cylinders," 15th AIAA/CEAS Aeroacoustics Conf., Miami, FL, AIAA Paper 2009-3275, May 2009.
- [16] Hutcheson, F., and Brooks, T., "Noise Radiation from Single and Multiple Rod Configurations," AIAA Paper 2006-2629, 2006.
- [17] Choi, H., Jeon, W.-P., and Kim, J., "Control of Flow over a Bluff Body," *Annual Review of Fluid Mechanics*, Vol. 40, 2008, pp. 113–129.  
doi:10.1146/annurev.fluid.39.050905.110149
- [18] Amitay, M., Smith, B. L., and Glezer, A., "Aerodynamic Flow Control Using Synthetic Jet Technology," 36th AIAA Aerospace Sciences Meeting, Reno, NV, AIAA Paper 98-0208, 1998.
- [19] Corke, T. C., Post, M. L., and Orlov, D. M., "Single Dielectric Barrier Discharge Plasma Enhanced Aerodynamics: Physics, Modeling and Application," *Experiments in Fluids*, Vol. 46, 2008, pp. 1–26.  
doi:10.1007/s00348-008-0582-5
- [20] Moreau, E., "Airflow Control by Non-Thermal Plasma Actuators," *Journal of Physics D: Applied Physics*, Vol. 40, pp. 605–636.  
doi:10.1088/0022-3727/40/3/S01
- [21] Thomas, F. O., Corke, T. C., Iqbal, M., Kozlov, A., and Schatzman, D., "Optimization of SDBD Plasma Actuators for Aerodynamic Flow Control," *AIAA Journal*, Vol. 47, No. 9, 2009, pp. 2169–2178.  
doi:10.2514/1.41588
- [22] Thomas, F. O., Kozlov, A., and Corke, T. C., "Plasma Actuators for Cylinder Flow Control and Noise Reduction," *AIAA Journal*, Vol. 46, No. 8, 2008, pp. 1921–1931.  
doi:10.2514/1.27821
- [23] Kim, D., and Wang, M., "Large-Eddy Simulation of Flow Over a Circular Cylinder with Plasma-Based Control," AIAA Paper 2009-1080, 2009.
- [24] Huang, X., and Li, Y., "Broadband Flow-Induced Sound Control Using Plasma Actuators," *Journal of Sound and Vibration*, Vol. 329, 2010, pp. 2477–2489.  
doi:10.1016/j.jsv.2010.01.018
- [25] Huang, X., Chan, S., and Zhang, X., "An Atmospheric Plasma Actuator," *IEEE Transactions on Plasma Science*, Vol. 35, No. 3, 2007, pp. 693–695.  
doi:10.1109/TPS.2007.896781
- [26] Fridman, A., and Kennedy, L. A., *Plasma Physics and Engineering*, Taylor & Francis, New York, 2004.



- [27] Enloe, C. L., McLaughlin, T. E., VanDyken, R. D., Kachner, K. D., Jumper, E. J., Corke, T. C., Post, M., and Haddad, O., "Mechanisms and Responses of a Single Dielectric Barrier Plasma Actuator: Geometric Effects," *AIAA Journal*, Vol. 42, No. 3, 2004, pp. 595–604. doi:10.2514/1.3884
- [28] Enloe, C. L., McLaughlin, T. E., VanDyken, R. D., Kachner, K. D., Jumper, E. J., and Corke, "Mechanisms and Responses of a Single Dielectric Barrier Plasma Actuator: Plasma Morphology," *AIAA Journal*, Vol. 42, No. 3, 2004, pp. 589–594. doi:10.2514/1.2305
- [29] Gibalov, V. I., and Pietsch, G. J., "The Development of Dielectric Barrier Discharges in Gas Gaps and on Surfaces," *Journal of Physics D: Applied Physics*, Vol. 33, 2000, pp. 2618–2636. doi:10.1088/0022-3727/33/20/315
- [30] Raizer, Yu. P., *Gas Discharge Physics*, Springer-Verlag, Berlin, 1991.
- [31] Schatzman, D. M., and Thomas, F. O., "Turbulent Boundary Layer Separation Control Using Plasma Actuators," *AIAA Journal*, Vol. 48, No. 8, 2010, pp. 1620–1634. doi:10.2514/1.J050009
- [32] Huang, J., Corke, T. C., and Thomas, F. O., "Plasma Actuators for Separation Control of Low-Pressure Turbine Blades," *AIAA Journal*, Vol. 44, No. 1, 2006, pp. 51–57. doi:10.2514/1.2903
- [33] Huang, J., Corke, T. C., and Thomas, F. O., "Unsteady Plasma Actuators for Separation Control of Low-Pressure Turbine Blades," *AIAA Journal*, Vol. 44, No. 7, 2006, pp. 1477–1487. doi:10.2514/1.19243

A. Naguib  
Associate Editor

**This article has been cited by:**

1. Ronald E. Hanson, Kyle M. Bade, Brandt A. Belson, Philippe Lavoie, Ahmed M. Naguib, Clarence W. Rowley. 2014. Feedback control of slowly-varying transient growth by an array of plasma actuators. *Physics of Fluids* **26**:2, 024102. [[CrossRef](#)]
2. Jin-Jun Wang, Kwing-So Choi, Li-Hao Feng, Timothy N. Jukes, Richard D. Whalley. 2013. Recent developments in DBD plasma flow control. *Progress in Aerospace Sciences* **62**, 52-78. [[CrossRef](#)]
3. Timothy N. Jukes, Kwing-So Choi. 2013. On the formation of streamwise vortices by plasma vortex generators. *Journal of Fluid Mechanics* **733**, 370-393. [[CrossRef](#)]
4. Stanislav V. Gordeyev, Flint O. Thomas. 2013. A temporal proper decomposition (TPOD) for closed-loop flow control. *Experiments in Fluids* **54**:3. . [[CrossRef](#)]
5. Samik Bhattacharya, James Gregory The Optimum Wavelength of Spanwise Segmented Plasma Actuator Forcing of a Circular Cylinder Wake . [[Citation](#)] [[PDF](#)] [[PDF Plus](#)]
6. Jee Hann Ng, Jiun-Ming Li, Yongdong Cui, T.t. Lim Active Flow Control on a Circular Cylinder via Streamwise-oriented Dielectric Barrier Discharge Plasma Actuators . [[Citation](#)] [[PDF](#)] [[PDF Plus](#)]
7. Jonas Moeck, Deanna Lacoste, Christophe Laux, Christian Paschereit Control of combustion dynamics in a swirl-stabilized combustor with nanosecond repetitively pulsed discharges . [[Citation](#)] [[PDF](#)] [[PDF Plus](#)]
8. E. P. DeMauro, C. M. Leong, M. Amitay. 2013. Interaction of a synthetic jet with the flow over a low aspect ratio cylinder. *Physics of Fluids* **25**:6, 064104. [[CrossRef](#)]
9. Edward Demauro, Chia Leong, Michael Amitay Interaction of a Single Synthetic Jet with a Finite Aspect Ratio Circular Cylinder . [[Citation](#)] [[PDF](#)] [[PDF Plus](#)]
10. Samik Bhattacharya, James Gregory Effect of Three-Dimensional Plasma Actuation on the Wake of a Circular Cylinder . [[Citation](#)] [[PDF](#)] [[PDF Plus](#)]